7078–7093 *Nucleic Acids Research, 2019, Vol. 47, No. 13* *Published online 25 May 2019*
doi: 10.1093/nar/gkz454

The structure of human EXD2 reveals a chimeric 3′ to 5′ exonuclease domain that discriminates substrates via metal coordination

Jumi Park[1,7,†], Song-Yi Lee[2,3,†], Hanbin Jeong[1,7], Myeong-Gyun Kang[2], Lindsey Van Haute[4], Michal Minczuk[4], Jeong Kon Seo[5], Youngsoo Jun[6,7], Kyungjae Myung[1,8], Hyun-Woo Rhee[3,*] and Changwook Lee[1,7,8,*]

[1]Department of Biological Sciences, School of Life Sciences, Ulsan National Institute of Science and Technology, 50 UNIST-gil, Ulsan 44919, Republic of Korea, [2]Department of Chemistry, Ulsan National Institute of Science and Technology, 50 UNIST-gil, Ulsan 44919, Republic of Korea, [3]Department of Chemistry, Seoul National University, Seoul 08826, Republic of Korea, [4]MRC Mitochondrial Biology Unit, University of Cambridge, Cambridge CB2 0XY, UK, [5]UNIST Central Research Facilities (UCRF), Ulsan National Institute of Science and Technology, 50 UNIST-gil, Ulsan 44919, Republic of Korea, [6]School of Life Sciences, Gwangju Institute of Science and Technology, Gwangju 61005, Republic of Korea, [7]Cell Logistics Research Center, Gwangju Institute of Science and Technology, Gwangju 61005, Republic of Korea and [8]Center for Genomic Integrity, Institute for Basic Science (IBS), Ulsan 44919, Republic of Korea

Received April 17, 2019; Revised May 07, 2019; Editorial Decision May 09, 2019; Accepted May 10, 2019

ABSTRACT

EXD2 (3′-5′ exonuclease domain-containing protein 2) is an essential protein with a conserved DEDDy superfamily 3′-5′ exonuclease domain. Recent research suggests that EXD2 has two potential functions: as a component of the DNA double-strand break repair machinery and as a ribonuclease for the regulation of mitochondrial translation. Herein, electron microscope imaging analysis and proximity labeling revealed that EXD2 is anchored to the mitochondrial outer membrane through a conserved N-terminal transmembrane domain, while the C-terminal region is cytosolic. Crystal structures of the exonuclease domain in complex with Mn^{2+}/Mg^{2+} revealed a domain-swapped dimer in which the central α5–α7 helices are mutually crossed over, resulting in chimeric active sites. Additionally, the C-terminal segments absent in other DnaQ family exonucleases enclose the central chimeric active sites. Combined structural and biochemical analyses demonstrated that the unusual dimeric organization stabilizes the active site, facilitates discrimination between DNA and RNA substrates based on divalent cation coordination and generates a positively charged groove that binds substrates.

INTRODUCTION

EXD2 (3′-5′ exonuclease domain-containing protein 2) was identified as a new component that plays an essential role in mediating the repair of DNA double-strand breaks (1). It was suggested that EXD2 might be required to facilitate DNA end resection during homologous recombination by functionally interacting with the MRE11-RAD50-NBS1 (MRN) complex. Primary structure analysis revealed a 3′ to 5′ exonuclease domain belonging to the DnaQ (DEDDy) family sharing high sequence similarity with the exonuclease domain of Werner syndrome protein (WRN), an enzyme involved in maintaining genome stability, and recombinant EXD2 exhibits 3′ to 5′ exonuclease activity against DNA *in vitro* (1).

However, in contrast to previous results, database analysis using The Human Protein Atlas (www.proteinatlas.org) (2), a public resource of immunofluorescence images for the human proteome, raised the possibility that EXD2 might be localized to mitochondria in various mammalian cell lines such as A-431, U-2 OS and U-251 MG. Supporting this possibility, Hensen *et al.* recently reported that EXD2 is predominantly associated with the mitochondrial outer membrane (3). Meanwhile, Stracker and colleagues suggested that EXD2 is localized to the inner mitochondrial membrane (IMM) or matrix (4). According to the report, EXD2 is a mitochondrial ribonuclease that plays important roles in mitochondrial functions such as respiration,

*To whom correspondence should be addressed. Tel: +82 52 217 2534; Fax: +82 52 217 2639; Email: changwook@unist.ac.kr
Correspondence may also be addressed to Hyun-Woo Rhee. Email: rheehw@snu.ac.kr
†The authors wish it to be known that, in their opinion, the first two authors should be regarded as Joint First Authors.

ATP production and mitochondrial translation. The sub-location of EXD2 within mitochondria was examined using proteinase K digestion of purified mitochondria in combination with electron microscopy (EM) imaging following staining with immuno-gold (4). However, such conventional approaches based on protease accessibility of the sub-mitochondrial proteome in purified mitochondria can lead to mis-interpretation if the target protein is unexpectedly resistant to proteases, as demonstrated for NDUFB10 (5). Furthermore, immuno-gold EM imaging requires cellular permeabilization, which occasionally degrades cellular ultrastructure (6), and treatment with immuno-gold may cause unintended extraction or relocalization of proteins (7).

Interestingly, EXD2 exhibited exonuclease substrate discrimination activity depending on the metal cofactors coordinated (4). In the presence of $MnCl_2$, EXD2 displays comparable activity toward DNA and RNA substrates, but activity toward DNA substrates is significantly reduced when $MgCl_2$ is used as a cofactor. This is an interesting result because substrate discrimination via divalent cations bound to exonucleases is a novel feature shown only for EXD2. Even in WRN exonuclease, which shares high sequence similarity with EXD2, metal cofactor-driven substrate discrimination has not been observed (8,9). Moreover, given that EXD2 acts as a ribonuclease in mitochondria rather than the nucleus, this could be advantageous and allow EXD2 to modulate its activity against DNA or RNA (4). However, it remains unknown exactly how the exonuclease activity of EXD2 toward DNA substrates is specifically limited in the presence of the Mg^{2+} cation, considered the likely physiological metal ion within cells. Therefore, molecular-level studies on EXD2 are needed to explore these distinctive features.

In the present study, we demonstrated that EXD2 is an outer mitochondrial membrane (OMM) protein anchored to the membrane through the N-terminal transmembrane (TM) domain, while most of the functional region, including the exonuclease domain, faces the cytosol. Furthermore, we determined crystal structures of the exonuclease domain of EXD2 in complex with Mn^{2+}/Mg^{2+} and (d)GMP, revealing a novel molecular mechanism by which EXD2 can distinguish DNA or RNA substrates depending on metal coordination, unlike other DnaQ family exonucleases reported to date.

MATERIALS AND METHODS

Mammalian cell culture and transfection

HEK293 cells from the Korean Cell Line Bank (Seoul, Korea) were cultured in Dulbecco's modified Eagle's medium (DMEM; Gibco) supplemented with 10% fetal bovine serum (FBS), 50 units/ml penicillin and 50 μg/ml streptomycin at 37°C under 5% CO_2. HeLa cells from the Korean Cell Line Bank were cultured in the same conditions. Cells were transfected at 60–80% confluence using Lipofectamine 2000 (Life Technologies) according to the manufacturer's instructions.

Fluorescence microscopy imaging

At 18–24 h after transfection in HeLa cells, the medium of the EXD2-V5-APEX2-transfected sample was changed to fresh growth medium containing 500 μM biotin-phenol. This culture was incubated for 30 min and labeled according to a previously published protocol (10). Next, H_2O_2 was added to a final concentration of 1 mM, and the plate was gently agitated for 1 min at room temperature. The reaction was quenched by washing twice with Quencher solution consisting of Dulbecco's phosphate-buffered saline (DPBS) containing 5 mM Trolox, 10 mM sodium azide and 10 mM sodium ascorbate. The biotin labeling step was omitted for Non-APEX2 samples. Biotin-labeled and non-labeled cells were fixed with 4% paraformaldehyde. Cells were then washed with DPBS and permeabilized with cold methanol at −20°C for 5 min. Cells were washed again with DPBS and blocked for 1 h with blocking solution consisting of 2% bovine serum albumin (BSA) in TRIS-buffered saline with Tween 20 (TBST) at room temperature.

To detect APEX2-fusion expression, cells were incubated with both mouse anti-V5 antibody (Invitrogen, cat. no. R960-25, 1:5000 dilution) and rabbit anti-TOM20 (Santa Cruz, cat. no. sc-11415, 1:200 dilution) as a mitochondrial marker for 1 h at room temperature. To detect Flag-tagged EXD2 expression, cells were incubated with both mouse anti-Flag antibody (Sigma Aldrich, cat. no. F1804, 1:3000 dilution) and rabbit anti-TOM20 for 1 h at room temperature. After washing with TBST, cells were simultaneously incubated with secondary Alexa Fluor 568 goat anti-mouse IgG (Invitrogen, cat. no. A-11004, 1:1000 dilution) and Alexa Fluor 488 goat anti-rabbit IgG (Invitrogen, cat. no. A-11008, 1:1000 dilution) for 30 min at room temperature. SA-Alexa Fluor 647 IgG (Invitrogen, cat. no. S32357, 1:1000 dilution) was incubated with biotin-labeled samples in dialyzed blocking solution. Cells were then washed with TBST and maintained in DPBS on ice for imaging using an FV1000SPD instrument (Olympus) at the UNIST Optical Biomed Imaging Center (UOBC) in the Ulsan National Institute of Science and Technology (UNIST), Korea.

Transmission electron microscopy (TEM) imaging

Cells transiently expressing EXD2-V5-APEX2 or $EXD2^{1–37}$-V5-APEX2 were grown in plastic six-well plates (Falcon, 353078) to 90% confluence. Cells were fixed and stained with diaminodenzidine (DAB) according to a previously published method (5). Briefly, cells were fixed using 2% glutaraldehyde and 2% paraformaldehyde in 0.1 M sodium cacodylate buffer pH 7.4 over 30–60 min. Unreacted glutaraldehyde was quenched by 20 mM glycine and cells were washed again in cold buffer. Freshly diluted 1 mg/ml (2.8 mM) DAB and 10 mM H_2O_2 in phosphate-buffered saline (PBS) were added. After 20 min, cells were again washed with PBS. Post-fixation was performed using 2% (w/v) osmium tetroxide (Electron Microscopy Sciences) for 40 min on ice and cells were rinsed with chilled distilled water. Cells were brought to room temperature, washed with distilled water, carefully scraped, resuspended and centrifuged at 1500 × *g* for 1

min. The pellet was dehydrated in a graded ethanol series (50−100%) for 15 min for each step. The sample was then mixed 1:1 (v/v) with EMBED-812 resin (Electron Microscopy Sciences) and anhydrous ethanol for 1 h. The mixture was incubated overnight in 2:1 (v/v) resin and then exchanged with 100% resin for 2 h before transferring to fresh resin, followed by polymerization at 60°C for 24 h. Embedded cell pellets were cut with a diamond knife into 50 nm sections and imaged on a FEI-Tecnai G2 Spirit Bio Twin TEM instrument (operated at 120 kV) at the Korea Basic Science Institute in Chuncheon, Korea.

TOM20-pBirA stable cell line selection, culturing and labeling

Flp-In T-REx 293 cells (Life Technologies) were cultured under the same conditions as HEK293 cells. Stable cell generation, culturing and labeling were performed according to previously published methods (5). Briefly, stable cell lines were generated by co-transfection with the pcDNA 5/FRT/TO expression construct and the pOG44 plasmid (1:9). After 24 h of transfection, cells were treated with an appropriate concentration of hygromycin B (100−200 μg/ml). Media containing hygromycin B were changed every 3−4 days. After 2−3 weeks, 3−4 colonies were picked and cultured continuously. To induce protein expression and biotin labeling of stable cells, cells at 60−80% confluence were treated with 100 ng/ml doxycycline (Sigma Aldrich) and 50 μM biotin. After incubation for 18−24 h, cells were lysed for subsequent analyses.

TOM20-pBirA mass spectrometry (MS) sample preparation

MS sample preparation was carried out according to a previously published method (11). Briefly, after biotin labeling overnight, cells were washed several times with DPBS and lysed with 1.5 ml of RIPA lysis buffer, 1× protease inhibitor cocktail (Sigma Aldrich, cat. no. P8849) and 1 mM phenylmethylsulphonyl fluoride (PMSF) for 10 min at 4°C. Lysates were clarified by centrifugation and samples from two T75 flasks were combined (∼3 ml).

For removal of free biotin, 3 ml of cell lysate was filtered with an Amicon filter (Merck Millipore, UFC801096) three times using PBS containing 1 mM PMSF and 1× protease inhibitor cocktail. The final ∼1 ml concentrated cell lysate was transferred to a 1.5 ml Lobind tube and 300 μl of washed SA-beads (Pierce) were added. After rotating for 1 h, beads were washed twice with PBS, and after removing PBS, samples were denatured in 100 μl denaturing solution (6 M urea, 2 M thiourea, 10 mM HEPES). The solution was reduced using 20 μl of 100 mM dithiothreitol (DTT) in 50 mM ammonium bicarbonate (ABC) at 56°C. Alkylation was performed by adding 35 μl of 300 mM iodoacetamide in 50 mM ABC in the dark. The sample was diluted with 50 mM ABC to 1 ml. Trypsin digestion was performed by adding 8 μl of 1 mg/ml trypsin. The solution was incubated at 37°C with shaking at 900 rpm overnight. Beads were washed with PBS four times and eluted by boiling at 95°C for 10 min after adding 250 μl of 95% formamide and 10 mM EDTA (pH 8.2), and 750 μl of 3% (v/v) acetonitrile/0.1% (v/v) formic acid was added to a final volume of 1 ml. The solution was desalted using a Varian Bond ELUT column (Agilent, 12109301).

MS detection of labeled peptides and data processing

An LTQ-Orbitrap mass spectrometer (Thermo, Bremen, Germany) equipped with a nanoelectrospray ion source was employed for MS detection. All MS analyses and data processing were performed as described previously (11).

Cloning, protein expression and purification

DNA fragments encoding a highly soluble construct of human EXD2 (residues 76−564, tEXD2) and the 3′-5′ exonuclease domain (residues 76−295, EXD2-exo) were amplified by PCR using *Homo sapiens* cDNA as template and cloned into the pcDNA5, pET28b-SMT3 and pETDUET-1 vectors. The resulting pcDNA5 constructs were used in mammalian transfection for imaging and pull-down experiments. The pETDUET-1 vector was previously modified to include a tobacco etch virus (TEV) protease cleavage site before the first amino acid of the EXD2 protein. Expression plasmids were transformed into *Escherichia coli* BL21 (DE3) competent cells, protein expression was induced with 0.3 mM isopropyl-β-D-1-thiogalactopyranoside (IPTG) when cells reached an absorbance at 600 nm ($OD_{600\,nm}$) of 0.6 and culturing was continued at 18°C for 18 h. Cells were harvested by centrifugation at 3200 × *g* for 18 min and resuspended in buffer containing 25 mM sodium phosphate pH 7.8, 400 mM sodium chloride and 10 mM imidazole. After cell lysis by sonication, tEXD2 and EXD2-exo proteins were purified by Ni^{2+}-immobilized metal affinity chromatography (IMAC). The His_6-SMT3 tag of tEXD2 and the His_6 tag of EXD2-exo were cleaved by Ulp1 protease and TEV protease at a ratio of 1:500 and 1:30 (w/w), respectively, during dialysis against 25 mM TRIS-HCl, pH 7.5, 150 mM NaCl and 4 mM β-mercaptoethanol at 4°C overnight. Cleaved tags and non-cleaved fusion proteins were removed by a second round of Ni^{2+}-IMAC. For further purification, proteins were applied to a Superdex 200 column (GE Healthcare) equilibrated with 25 mM TRIS-HCl, pH 7.5, 150 mM NaCl and 5 mM DTT. Proteins were concentrated to 10 mg/ml and flash-frozen at −80°C for later use. All point mutants and deletion mutants were generated by PCR-based mutagenesis, and mutations were confirmed with DNA sequencing. All mutants were purified as described above.

Crystallization and structure determination

Crystals grew when EXD2-exo was mixed with an equal volume of reservoir liquor containing 18% (w/v) polyethylene glycol (PEG) 8000, 100 mM 2-(N-morpholino)ethanesulfonic acid, pH 6.0, 0.2 M calcium acetate and 5 mM DTT by the hanging-drop vapor diffusion method at 4°C. Crystals were cryoprotected by transferring into a reservoir solution augmented with 30% (v/v) ethylene glycol and flash-frozen in liquid nitrogen. X-ray diffraction data were collected at beamline 5C of the Pohang Accelerator Laboratory at 100 K. The best crystals diffracted to 1.6 Å resolution and complete datasets were

processed using HKL2000 (12). Phases were calculated by molecular replacement using Phaser in the Phenix suite (13) with the coordinates of WRN-exo (PDB ID: 2FBT) as a search model. Phaser found two EXD2 molecules in the asymmetric unit of the $P2_12_12_1$ space group. Model building and refinement were performed using Coot (14) and Phenix refine (15), respectively. The R_{free} of the refined model was 21.95%. The following residues of EXD2-exo were disordered in the electron density map and therefore not modeled: residue 76, residues 219–222, residues 261–274 and residue 295 in the first copy; residue 76, residues 219–223, residues 261–274 and residues 293–295 in the second copy.

To solve the metal-coordinated structures, crystals of EXD2-exo were transferred to reservoir solution supplemented with 20–50 mM $MnCl_2$ or $MgCl_2$ and 5 mM dGMP or GMP for at least 1 day, and flash-frozen in liquid nitrogen. Structures were solved by difference Fourier methods. To reduce the effect of model bias, we refined the protein chains without water molecules and ions using simulated annealing before calculating difference maps for detection of positive peaks corresponding to ions and solvent molecules. Model building and refinement were performed as described above. Detailed crystallographic data and data processing and refinement statistics are summarized in Supplementary Table S1.

In vitro exonuclease activity assay

In vitro nuclease activity assays were conducted as reported previously (1). In our experiments, DNA or RNA substrates were labeled using 5-fluorescein amidite (5-FAM) at the 5′ end instead of [γ-^{32}P] 5′ labeling. DNA or RNA substrates at a concentration of 0.25 μM were incubated with 0.05–0.2 μM or 0.5–1.5 μM tEXD2, or 0.5–2 μM or 20–60 μM EXD2-exo, for 30 min at 37°C in reaction buffer consisting of 20 mM HEPES-KOH, pH 7.5, 50 mM KCl, 0.5 mM DTT, 0.05% (v/v) Triton X-100, 0.1 mg/ml BSA, 5% (v/v) glycerol, 1 mM ATP and 5 mM metal ions ($MnCl_2$, $MgCl_2$, $ZnCl_2$ or $CaCl_2$) or without metals. After reaction, products were separated by non-denaturing 15% TRIS/Borate/EDTA-polyacrylamide gel electrophoresis (TBE-PAGE) and fluorescence was detected using an ImageQuant LAS 4000 instrument (GE Healthcare).

Size exclusion chromatography (SEC) analysis

Analysis of the relative molecular mass (Figures 2C and 3D; Supplementary Figure S4A) was carried out by SEC. Proteins were concentrated to 15–20 mg/ml and injected onto a Superdex 200 16/60 column (GE Healthcare) equilibrated with buffer containing 25 mM TRIS-HCl, pH 7.5, 150 mM NaCl and 5 mM DTT.

Pull-down assay

For pull-down assays, cells were prepared in a six-well plate. Full-length human EXD2-V5-Avitag (1000 ng), EXD2-Flag (1000 ng) and BirA-NES (500 ng) were co-transfected in HEK293 cells. After overnight biotinylation following addition of 10 μM biotin, cells were lysed with 200 μl of Cell Extraction Buffer (Life Technologies, cat. no. FNN0011) containing 1× protease inhibitor cocktail (Sigma Aldrich, cat. no. P8849) and 1 mM PMSF for 30 min at 4°C. Lysates were transferred into Eppendorf tubes, vortexed for 2 min and clarified by centrifugation at 15 000 × *g* for 10 min at 4°C.

A 20 μl of SA magnetic beads (Invitrogen, cat. no. 88816) were incubated with 170 μl of cell lysate for 1 h. The flow-through (FT) fraction was retained and beads were washed three times with Cell Extraction Buffer. Biotinylated EXD2-V5-Avitag was eluted with 2× Laemmli buffer (BioRad, cat. no. 161-0737) supplemented with 20 mM DTT and 2 mM biotin by heating to 95°C for 10 min. Crude and elution samples were separated by 10% sodium dodecyl sulphate (SDS)-PAGE and transferred to a nitrocellulose membrane that was subsequently stained with 0.1% Ponceau S in 5% acetic acid/water for 10 min. After blocking with 2% (w/v) BSA and 0.1% Tween 20 in TBST at 4°C overnight or at room temperature for 1 h, blots were immersed in anti-V5 (Invitrogen, cat. no. R960-25, 1:5000 dilution) or anti-Flag (Sigma Aldrich, cat. no. F1804, 1:3000 dilution) in blot blocking buffer at room temperature for 60 min, then rinsed with blot blocking buffer four times for 5 min each time. Blots were then immersed in secondary antibody (anti-mouse-HRP, BioRad, cat. no. 1721011) in blot blocking buffer for between 30 min and 1 h at room temperature. Membranes were then washed again for 4 × 5 min in TBST before imaging with Clarity reagent (BioRad) on a G:BOX Chemi XRQ instrument (Syngene).

Circular dichroism (CD) spectroscopy

Secondary structures of EXD2-exo, EXD2$^{76–284}$ and EXD2$^{76–260}$ were monitored by CD spectroscopy on a Jasco J-815 instrument (Jasco, UK) from 190 to 260 nm. Conformational changes were also monitored by CD spectroscopy with temperature scanning from 25 to 90°C over a 13 min period with detection at 222 nm. Protein samples for wavelength scans (0.2 mg/ml) and temperature scans (1 mg/ml) were prepared in 25 mM sodium phosphate pH 7.5 with 150 mM sodium fluoride and 5 mM β-mercaptoethanol.

RESULTS

EXD2 is a mitochondrial outer membrane protein facing the cytosol

Hydropathy plot analysis strongly indicated that EXD2 might contain a single TM domain comprising residues 1–37 at the N-terminus (Supplementary Figure S1A). Since several previous studies reported that the N-terminal single TM domain could function as a signal motif for targeting to mitochondria (16,17), we tested whether this domain is crucial for mitochondrial targeting of EXD2. For this experiment, we generated EXD2-Flag (Flag-tagged at the C-terminus) constructs and expressed them in cultured cells (Supplementary Table S2). Figure 1A shows that EXD2-Flag was obviously targeted to mitochondria, overlapping with TOM20 (Pearson correlation, $R = 0.94$). By contrast, Flag-EXD2 tagged at the N-terminus was not successfully

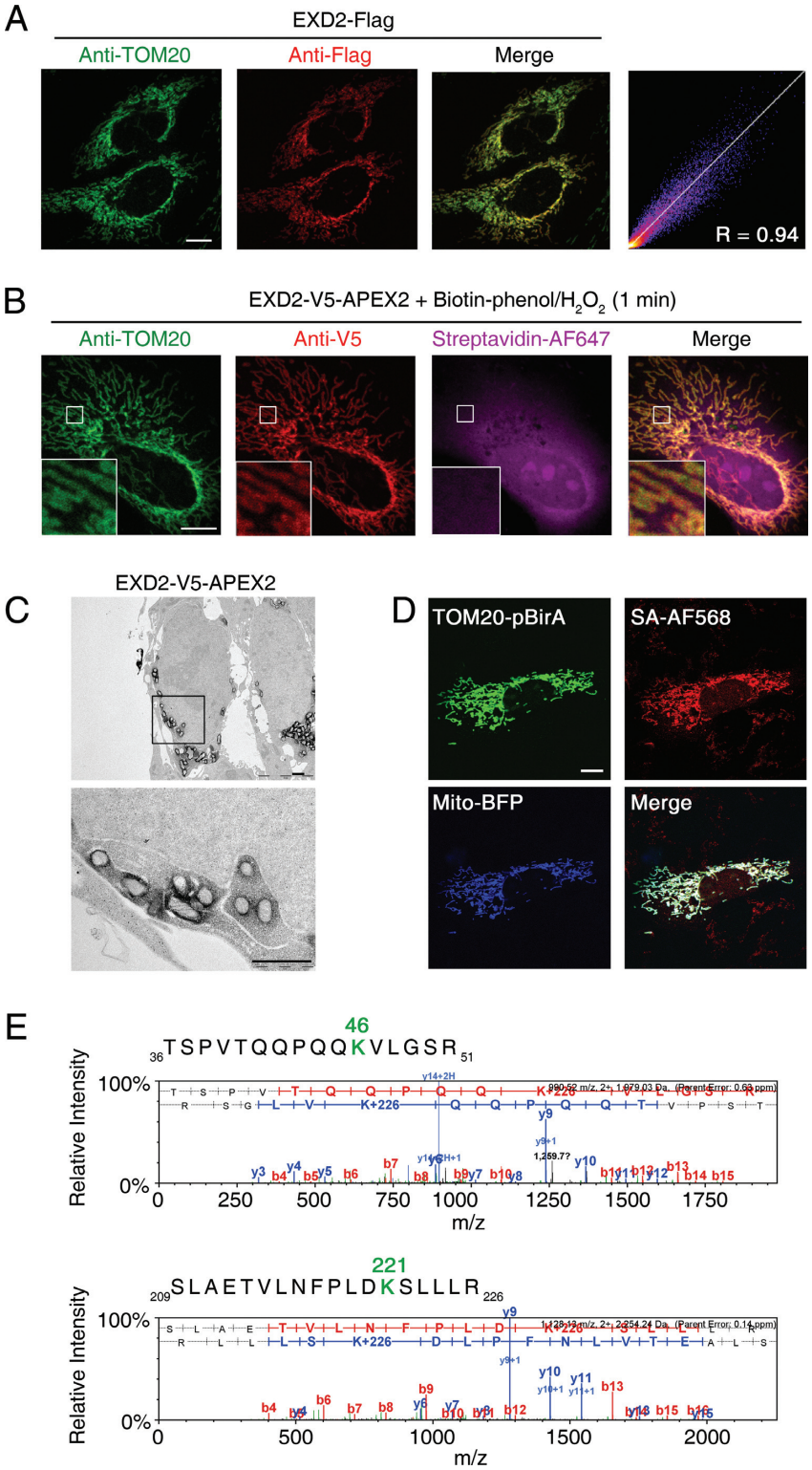

Figure 1. EXD2 has an N-terminal single transmembrane (TM) domain and is localized to the outer mitochondrial membrane (OMM). (**A**) Confocal microscopy imaging of EXD2-Flag in HeLa cells. The green channel (anti-TOM20) is a mitochondrial marker, and the red channel (anti-Flag) is for analysis of EXD2-Flag expression. Pearson correlation coefficient (R) = 0.94; scale bar = 10 μm. (**B**) Confocal microscopy imaging of EXD2-V5-APEX2 in HeLa cells. The green channel (anti-TOM20) is a mitochondrial marker, the red channel (anti-V5) is for analysis of EXD2-V5-APEX2 expression, and the magenta channel is the biotin-phenol labeling pattern; scale bar = 10 μm. (**C**) Electron microscopy (EM) imaging of EXD2-V5-APEX2 using the APEX2-EM method; scale bar = 1 μm. (**D**) Confocal microscopy imaging of TOM20-pBirA-HA expression in HeLa cells. The green channel (anti-HA) was used to analyze enzyme expression, the red channel (streptavidin, SA-AF568) to analyze the biotinylation pattern, and the blue channel to analyze the mitochondrial marker mito-BFP; scale bar = 10 μm. (**E**) Tandem mass spectrometry (MS/MS) spectra of biotin-labeled EXD2 peptides. Biotin-labeled lysine residues are colored green.

targeted to mitochondria (Supplementary Figure S1B), and the resulting correlation with TOM20 was low ($R = 0.43$). We also checked that EXD2$^{38–621}$-Flag, which includes the N-terminal TM domain-deleted EXD2 sequence, was also nuclear-localized in mammalian (HeLa) cells (Supplementary Figure S1C). This result indicates that the predicted N-terminal TM domain of EXD2 might play an important role in mitochondrial targeting, as shown for other signal-anchored proteins such as TOM20 or AKAP1 in which the N-terminal single TM domain acts as a signal-anchor peptide at the OMM (16,17).

To investigate the sub-mitochondrial localization of EXD2 in more detail, constructs encoding EXD2-V5-APEX2 and EXD2$^{1–37}$-V5-APEX2 were expressed in HeLa cells, which were stained with streptavidin (SA)-AF647 after biotinylation. As shown in Figure 1B, EXD2-V5-APEX2 was tightly localized to mitochondria and overlapped strongly with TOM20. However, APEX-mediated biotinylated pattern by EXD2-V5-APEX2 was not tightly localized to mitochondria and was instead diffusely distributed in the cytosol. We also observed a similar diffuse pattern for biotinylated EXD2$^{1–37}$-V5-APEX2 (Supplementary Figure S1D). This diffuse biotin labeling pattern in mitochondria was previously observed for several mitochondrial POI (protein of interest)-APEX2 constructs in which the C-terminus of POIs is localized to the outside of the IMM (10). To confirm whether EXD2 is localized to the mitochondrial inter-membrane space (IMS) or at the OMM, we prepared EM samples of EXD2-V5-APEX2 and EXD2$^{1–37}$-V5-APEX2 by following a protocol reported previously for APEX2-EM (18). As shown in Figure 1C, most diaminobenzidine (DAB) staining from EXD2-V5-APEX2 was observed at the OMM. Furthermore, the EM results for EXD2$^{1–37}$-V5-APEX2 yielded a similar OMM pattern (Supplementary Figure S1E). These results strongly indicate that the N-terminal single TM domain of EXD2 is incorporated at the OMM as a signal-anchor domain.

To further confirm the localization of endogenous EXD2 in the OMM, we employed Spot-BioID proximity labeling, which facilitates profiling of biotin-labeled peptides (11). This method can identify directly biotinylated protein candidates that can be considered as proximal proteins of POI-pBirA. We performed *in situ* biotinylation of OMM proteins using TOM20-pBirA, in which pBirA is located at the cytosolic face of the OMM (Figure 1D). After biotin labeling, total biotinylated proteins and peptides were enriched and analyzed by mass spectrometry (MS). Five lysine sites (K46, K221, K295, K562 and K611) of endogenous EXD2 were reproducibly biotinylated by TOM20-pBirA, and labeled residues are within the C-terminal region of the predicted TM domain, suggesting that the C-terminal region of EXD2, including the exonuclease domain, functions on the cytosolic face of the OMM (Figure 1E and Supplementary Figure S2).

To corroborate the results of proximity labeling, we performed cellular fractionation experiments of HEK293T cells. Endogenous EXD2 was clearly enriched within the mitochondrial fraction, along with mtSSB1 (a well-characterized mitochondrial matrix protein) and TOM22 (a protein localized in OMM) (Supplementary Figure S1F). While mtSSB1 were resistant to proteinase K treatment of the mitochondrial fraction, both EXD2 and TOM22 were degraded in similar conditions, consistent with localization of EXD2 in OMM (Supplementary Figure S1F). Taken together, our data clearly support the notion of EXD2 localizing at the OMM with signal anchored transmembrane domain.

Characterization and structure determination of EXD2

Previous biochemical studies showed that EXD2 exhibits a 3′ to 5′ exonuclease activity (1,4). To further characterize the exonuclease activity of EXD2 *in vitro*, we constructed a truncated version of EXD2 (residues 76−564, subsequently designated tEXD2; Figure 2A) that is reported to exhibit robust expression *in vitro* (1) and purified the protein to homogeneity. To test the exonuclease activity of tEXD2, single-stranded 50 nt DNA oligonucleotides labeled with 5-fluorescein amidite (5-FAM) at the 5′ end were incubated with tEXD2 for 30 min, and reaction products were separated by 15% non-denaturing TRIS/Borate/EDTA-polyacrylamide gel electrophoresis (TBE-PAGE) and subjected to fluorescence detection. Figure 2B shows that tEXD2 possesses 3′ to 5′ exonuclease activity. Interestingly, tEXD2 displayed metal-specific activity, with strong exonuclease activity only in the presence of Mn^{2+}, and no exonuclease activity with other divalent metal ions such as Mg^{2+}, Zn^{2+} and Ca^{2+}. From these results, we concluded that tEXD2 is a Mn^{2+}-specific 3′ to 5′ exonuclease targeting DNA substrates. Additionally, tEXD2 exhibited enzymatic activity against RNA substrates in the presence of both Mn^{2+} and Mg^{2+} ions, although activity was again stronger with Mn^{2+} ions (Supplementary Figure S3A).

To obtain further structural insight into the metal-specific exonuclease activity of EXD2, we attempted to crystallize the human tEXD2 protein. However, despite extensive screening, we failed to grow crystals suitable for X-ray diffraction experiments. Combined limited proteolysis and sequence conservation analyses of EXD2 from various species identified a compact exonuclease domain of EXD2 comprising residues 76−295 (designated EXD2-exo; Figure 2A). Size exclusion chromatography (SEC) analysis revealed that recombinant EXD2-exo was present in both monomeric and dimeric forms in an ∼50:50 ratio in solution (Figure 2C). Self-oligomerization was also apparent for tEXD2 when analyzed by SEC and analytical ultracentrifugation (AUC; Supplementary Figure S4). Interestingly, EXD2-exo collected from the monomer fractions displayed substantially reduced exonuclease activity in the presence of Mn^{2+} ions. For RNA substrates, monomeric EXD2-exo was inactive regardless of Mn^{2+} or Mg^{2+} metal ions, whereas dimeric EXD2-exo possessed activity comparable with that of tEXD2 against both DNA and RNA substrates (Figure 2D and Supplementary Figure S3B).

We only obtained crystals of dimeric EXD2-exo, and these crystals diffracted to 1.6 Å resolution using synchrotron radiation. The crystals belong to space group $P2_12_12_1$ and contain two EXD2-exo molecules in the asymmetric unit. A molecular replacement solution was obtained using human Werner-exo (WRN-exo, PDB ID: 2FBT),

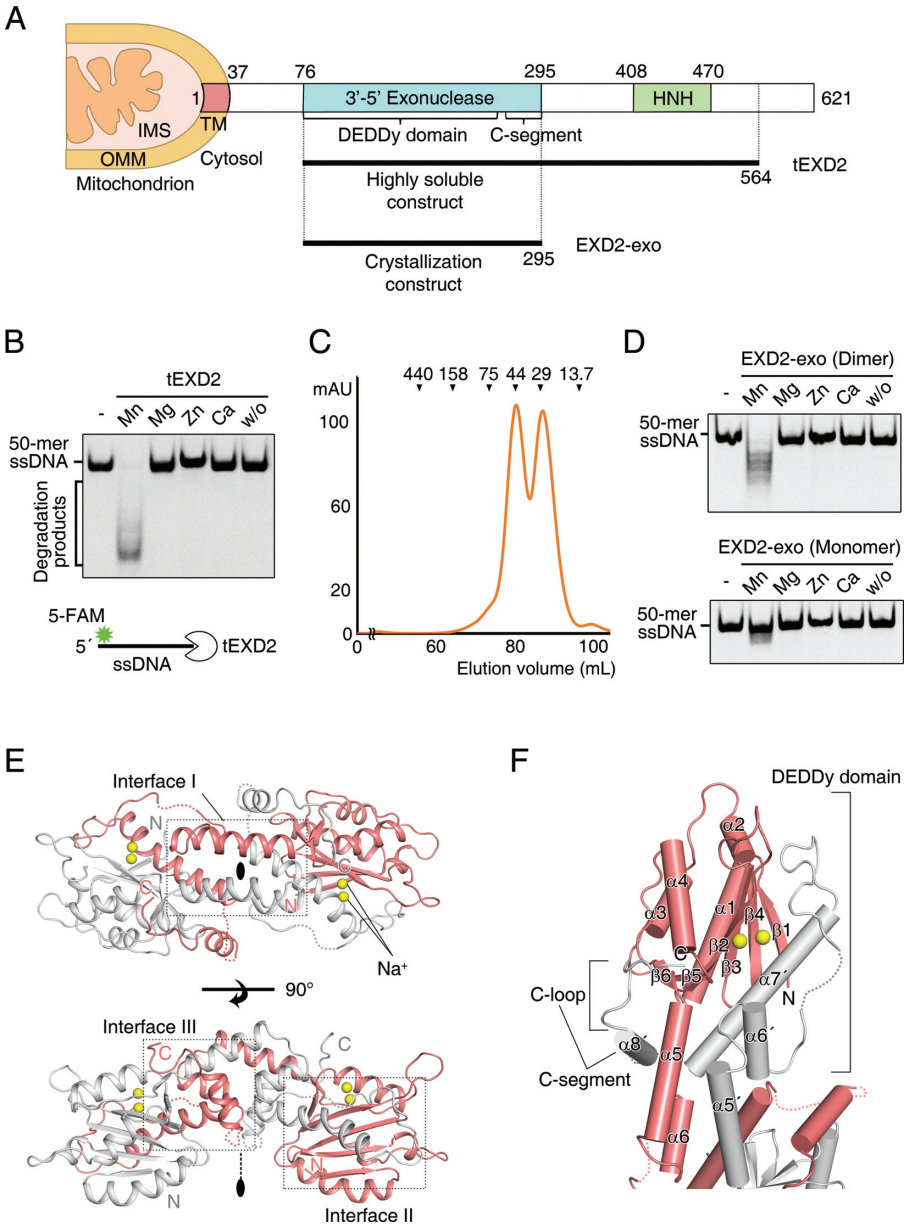

Figure 2. Crystal structure of EXD2-exo. (**A**) Schematic diagram showing the domain structure of human EXD2 and truncated constructs used in this study. Biochemical analyses revealed that EXD2 is anchored to the mitochondrial outer membrane (OMM) by a single TM domain at the N-terminus. The cytoplasmic portion of EXD2 contains a 3′-5′ exonuclease domain (residues 76–295) and a predicted HNH-like domain (residues 408–470). Based on the crystal structure, the 3′-5′ exonuclease domain consists of a canonical DEDDy domain followed by an additional C-segment; IMS, mitochondrial intermembrane space; OMM, mitochondrial outer membrane; TM, transmembrane domain. (**B**) Metal cation-dependent 3′-5′ exonuclease activity of tEXD2. A 0.2 μM sample of tEXD2 was incubated with 0.25 μM 5-fluorescein amidite (FAM)-labeled 50-mer single-stranded DNA (ssDNA) for 30 min at 37°C in 20 mM HEPES-KOH pH 7.5, 50 mM KCl, 0.5 mM dithiothreitol (DTT), 0.05% Triton X-100, 0.1 mg/ml BSA, 5% glycerol, 1 mM ATP and 5 mM metal ions ($MnCl_2$, $MgCl_2$, $ZnCl_2$ or $CaCl_2$) or without metal. Non-denaturing TRIS/Borate/EDTA-polyacrylamide gel electrophoresis (TBE-PAGE) showed that tEXD2 cleaves 5-FAM-labeled ssDNA only in the presence of $MnCl_2$. (**C**) Size exclusion chromatography (SEC) of EXD2-exo. EXD2-exo proteins were injected onto a Superdex 200 column (GE Healthcare) equilibrated in 25 mM TRIS-HCl, pH 7.5, 150 mM NaCl and 5 mM DTT. EXD2-exo was eluted in both dimeric and monomeric forms at an ∼50:50 ratio. Protein standards are shown above the chromatogram curves to compare the relative molecular mass (ferritin, 440 kDa; aldolase, 158 kDa; conalbumin, 75 kDa; ovalbumin, 44 kDa; carbonic anhydrase, 29 kDa; ribonuclease A, 13.7 kDa). (**D**) Metal cation-dependent 3′-5′ exonuclease activity of EXD2-exo. A 1.5 μM sample of each protein was mixed with 0.25 μM 5-FAM-labeled 50-mer ssDNA under the same conditions as in panel (**B**). (**E**) Overall structure of EXD2-exo in the crystallographic asymmetric unit. EXD2-exo forms a dimer through 2-fold rotational symmetry. Protomers are colored red and gray. The crystal structure was determined by molecular replacement (MR) and refined to 1.6 Å resolution (Supplementary Table S1). Three dimeric interfaces are highlighted with black dotted boxes (see also Supplementary Figure S7 for details). Yellow spheres indicate sodium ions bound to the active sites of EXD2-exo. (**F**) Ribbon diagram showing the DEDDy exonuclease domain of EXD2-exo. The EXD2-exo protomer consists of six β-strands and eight α-helices. The catalytic site of EXD2-exo is formed by the association of a central domain comprising β1–β6 and α1–α5 of one EXD2-exo molecule, and α6′–α7′ from the other molecule in the EXD2-exo dimer. A chimeric active site is formed by crossing over of the extended α5 helices between the two protomers of the dimer. The C-segments comprising swapped α8 helices and a well-ordered loop (C-loop, residues 285–294) enclose the exonuclease domain and stabilize the overall structure. All disordered regions are indicated by dotted lines.

which shares 28% sequence identity with EXD2-exo, as a search model. Successive rounds of model building and refinement resulted in an R_{work}/R_{free} of 0.192/0.220 with good stereochemistry (Supplementary Table S1).

Structure of EXD2-exo

Consistent with the biochemical analyses, EXD2-exo forms a dimer with overall dimensions of ∼91.0 × 42.7 × 39.3 Å, in which two molecules are arranged with a 2-fold rotational symmetry around the axis perpendicular to the plane (Figure 2E). No discernible differences were found in the two molecules, which have a root-mean square deviation (RMSD) of ∼0.253 Å for all Cα atoms. Each molecule consists of eight α-helices (α1−α8) and a six-stranded (β1−β6) β-sheet that folds into a canonical DnaQ-like exonuclease domain and contains two active site Na^+ ions, neither of which supports nuclease activity (Figure 2E and F; Supplementary Figure S5). Surprisingly, the α5−α7 helices are exchanged between molecules in the EXD2-exo dimer, resulting in a domain-swapped structure. Most interestingly, both exchanged α7 helices play a pivotal role in completing the exonuclease active sites in the opposing molecule in the EXD2-exo dimer. This unexpected structural perspective revealed why the exonuclease activity was significantly reduced in the EXD2-exo monomer (Figure 2D). This unusual conformation is a novel feature that is absent in other DnaQ family exonucleases. Although the structure of the EXD2-exo monomer itself cannot be exclusively superimposed with the exonuclease domains of DnaQ family proteins (RMSD > 3.0 Å), each complete composite monomeric exonuclease domain present in the EXD2-exo dimer strongly resembles the exonuclease domains of WRN, Klenow fragment (KF) and Ribonuclease D (Rnase D), with RMSD values for all Cα atoms of 1.035, 2.273 and 2.212 Å, respectively (Figure 3B and Supplementary Figure S6).

The crystal structure revealed that three direct interfaces are involved in the self-association of EXD2-exo, resulting in a buried surface area of 4024 $Å^2$ (Figure 2E and Supplementary Figure S7). The first interface is generated by a 2-fold arrangement of helices α5−α7 in the EXD2-exo dimer. In particular, helices α5 and α5′ from opposing molecules are organized in an antiparallel fashion, resulting in the formation of a coiled coil-like dimer (Figure 2E and Supplementary Figure S7, top). In addition, helix α5 also contacts both helix α6′ and the C-terminus of helix α7′ in a parallel fashion behind the α5–α5′ interface (Supplementary Figure S7, top left). Notably, the C-terminal ends of helices α7 and α7′ face each other, generating a precise 2-fold center in which the side chains of the two His256 residues are stacked side by side (Supplementary Figure S7, top right). The second interface is formed by an extensive contact between the exchanged loop (residues 227−237) followed by helix α7 (residues 238−260) and the central β-sheet of the active site in the opposing molecule, as described above (Figure 2E and Supplementary Figure S7, bottom left). In the third interface, the C-terminal fragment of EXD2-exo (designated as the C-segment) plays a critical role in the interaction, supporting structural integrity (Figure 2E and Supplementary Figure S7, bottom right). The active exonuclease domain of WRN-exo ends at residue 230, at the C-terminal end of helix α7 (9), whereas the equivalent helix α7 in EXD2-exo is followed by a flexible loop (residues 261−274) that is disordered, and this in turn is followed by the short helix α8 (residues 275−284) and a well-ordered loop (C-loop) comprising residues 285−294 (Figure 2E and F; Supplementary Figure S7, bottom right). Surprisingly, the two additional C-segments mutually enclose each other in the EXD2-exo dimer, and this clearly stabilizes the dimeric organization and assists the formation of stable active sites. In particular, the α8 helix associates with the C-terminus of α1′and α6′ and α5′ of the opposing molecule in the dimer (Figure 2F and Supplementary Figure S7, bottom right).

Residues 219−222 from the loop connecting helices α6 and α7, and residues 261–274 predicted to form an extended loop, are disordered in the structure. As discussed below, these apparently flexible regions might facilitate the binding of substrates and regulation of activity, respectively.

Extended helix α5 of EXD2-exo confers a domain-swapped structure

Sequence alignment of EXD2-exo with DnaQ family exonucleases including WRN, KF, RNase D, Exonuclease 1 (EXO1) and DNA polymerase III subunit epsilon (DPO3E) revealed that helix α5 of EXD2 is extended by five more residues (^{198}NNLLC^{202}) than in other compared exonucleases (Figure 3A) (9,19–22). This extended sequence is conserved in all EXD2 family members above metazoan species, suggesting that self-association through helix α5 might be evolutionally conserved and structurally important for EXD2 function (Supplementary Figure S5). The extended helix α5 clearly affects the overall conformation, and likely induces domain-swapped dimerization in EXD2-exo. Helices α5 and α6 of EXD2-exo are organized in an antiparallel manner, unlike the equivalent helices in other DnaQ family exonucleases, which are arranged in parallel pairs (Figure 3B and C; Supplementary Figure S6). Helices α6′ and α7′ from the opposing molecule in the EXD2-exo dimer can be perfectly superimposed with helices α5 and α7 of WRN-exo, suggesting that the dimeric configuration of EXD2-exo might not affect exonuclease activity (Figure 3C).

To examine the role of the α5 helix in dimer formation, we performed mutagenesis to disrupt the conformation of helix α5. Figure 3D shows that both single point (N198P) and deletion (residues Δ198−201) mutants of EXD2-exo eluted from the SEC column only as monomers, suggesting that the extended helix α5 is important for forming a domain-swapped dimer, as would be expected based on the crystal structure. We further tested if the mutants retained the ability to digest DNA, and observed that both mutants impaired exonuclease activity (Figure 3E). This result suggests that the formation of a swapped dimer is required for the catalytic activity of EXD2-exo.

Next, we examined whether full-length EXD2 also self-associates in live cells using pull-down assays (Figure 3F). For this experiment, we prepared mammalian expression constructs for $EXD2^{1–621}$ (full EXD2 sequence)-V5-Avitag (AP) and $EXD2^{1–621}$-Flag constructs. These constructs were co-expressed in HEK293 cells, and cytosol-targeted

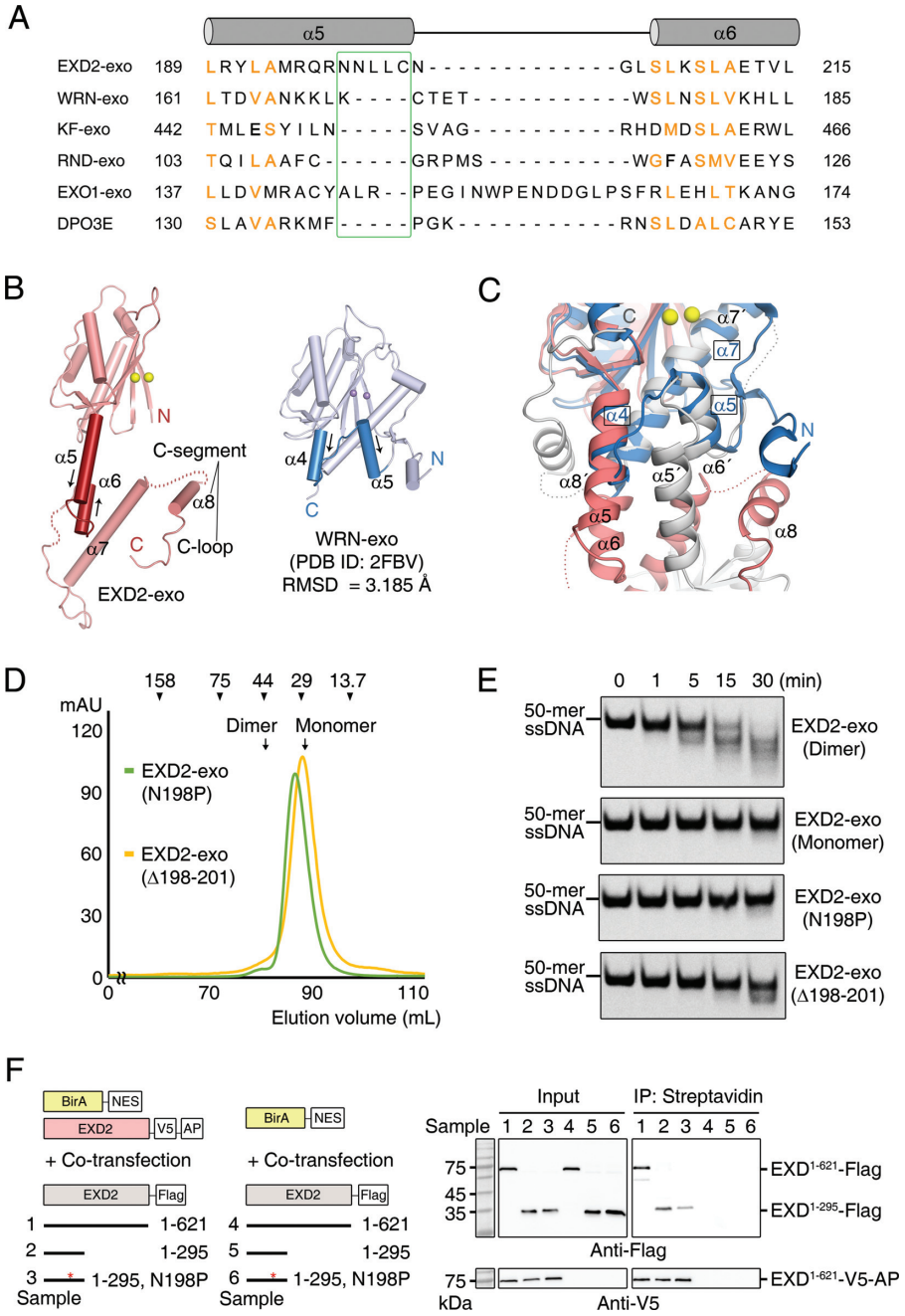

Figure 3. The extended α5 helix stabilizes a novel dimeric conformation in EXD2-exo. (**A**) Structure-based sequence alignment of helices α5 and α6 of human EXD2 and equivalent helices in other DnaQ family exonucleases including Werner syndrome ATP-dependent helicase (WRN, PDB ID: 2FBT), DNA polymerase I Klenow fragment (KF, PDB ID: 1KFS), ribonuclease D (RND, PDB ID: 1YT3), exonuclease 1 (EXO1, PDB ID: 1FXX) and DNA polymerase III subunit epsilon (DPO3E, PDB ID: 1J53). Sequence alignment reveals that the α5 helix is extended by five additional residues in EXD2 compared with other exonucleases (highlighted in the green box). Conserved residues are colored orange. (**B**) Structural comparison of EXD2-exo (red) and WRN-exo (blue) in ribbon representation positioned in the same orientation. Helices α4 and α5 of WRN-exo are arranged in a parallel manner (see arrows), but the equivalent helices (α5 and α6) in EXD2-exo are organized in an antiparallel fashion, resulting in significant conformational changes between helix α6 and the C-terminus (swapped in the EXD2-exo dimer; see also Supplementary Figure S6). (**C**) Close-up view of the structural superimposition of EXD2-exo and WRN-exo. To highlight the roles of helices α5−α7 of EXD2 in dimerization and formation of the active site, the structure of the composite exonuclease domain of EXD2 (red and gray) formed by domain swapping is aligned with the WRN-exo monomer (blue). Helices of WRN-exo are labeled in black boxes. (**D**) SEC chromatogram of EXD2-exo mutants N198P and Δ198−201. The experimental details are the same as in Figure 2C. (**E**) Time-dependent exonuclease activity of EXD2 mutants N198P and Δ198−201. A 1.5 μM sample of mutant protein was incubated with 0.25 μM 5-FAM-labeled 50-mer ssDNA for 1, 5, 15, or 30 min at 37°C and analyzed by non-denaturing TBE-PAGE. (**F**) EXD2 self-association assay in live cells. To analyze whether the full-length and exonuclease domain of EXD2 can physically associate in full-length EXD2 *in vivo*, full-length human EXD2-V5-Avitag (AP) was co-transfected with Flag-tagged full-length EXD2 ($EXD2^{1-621}$-Flag) or exonuclease domain of EXD2 ($EXD2^{1-295}$-Flag) in HEK293 cells (left, samples 1 and 2). The Avitag of EXD2-V5-AP can be biotinylated by co-transfection with BirA-NES (cytosol) for pull-down assays using SA-beads. Mutant version of the exonuclease domain ($EXD2^{1-295,\ N198P}$-Flag) was used as control (left, sample 3). As negative controls, the bait protein $EXD2^{1-621}$-V5-AP was omitted (left, samples 4, 5 and 6). Input is the crude sample before addition to SA-beads (right).

bacterial biotin ligase (BirA-NES) was also recombinantly expressed in the same cells for the selective biotinylation of Avitag of EXD2$^{1–621}$-V5-AP for streptavidin (SA)-bead pull-down (Figure 3F, left) (23). After biotinylation following addition of biotin (10 μM) overnight, cells were lysed and biotinylated EXD2$^{1–621}$-V5-AP was collected using SA-coated magnetic beads. Subsequent western blotting of anti-V5 revealed that enrichment of biotinylated EXD2$^{1–621}$-V5-AP was achieved using the SA-beads (Figure 3F, right, anti-V5 WB), and EXD2$^{1–621}$-Flag was also enriched using SA-beads bound to EXD2$^{1–621}$-V5-AP (Figure 3F, right, sample 1, anti-Flag WB). We also checked that EXD2$^{1–295}$-Flag, which contains the sequence of EXD2 from the N-terminal TM domain to the exonuclease domain, was also co-enriched with pulled-down EXD2$^{1–621}$-V5-AP (Figure 3F, right, sample 2, anti-Flag WB). However, in the same conditions, the enrichment level was significantly compromised for the N198P single point EXD2$^{1–295}$ mutant (EXD2$^{1–295,\ N198P}$-Flag), which was shown to be eluted exclusively as a monomer in SEC experiments (Figure 3F, right, sample 3, anti-Flag WB). We confirmed that the co-enrichment of Flag-tagged protein did not occur in negative control experiments lacking expression of the bait protein EXD2$^{1–621}$-V5-AP (Figure 3F, right, sample 4–6, anti-Flag WB). This result implies that the fully functionalized exonuclease domain of EXD2 forms a homodimer in live mammalian cells.

The EXD2-exo active site

Like other DEDDy superfamily exonucleases, EXD2-exo has two metal ions at the active site (Figure 4A, site A is referred to as [M_A] and site B is referred to as [M_B] in the crystal structure of EXD2-exo) (9). Although the crystallization solution contained 200 mM calcium acetate, sodium rather than calcium was bound to EXD2-exo, suggesting that Ca^{2+} is not a genuine ion supporting activity in EXD2-exo (Figure 4A and Supplementary Figure S8A). Indeed, EXD2 was inactive in the presence of calcium (Figure 2B and D). Consistent with other DEDDy exonucleases, two metal ions are coordinated by the catalytic core residues Asp108, Glu110, Asp171, Tyr242 and Asp246 (Figure 4A and Supplementary Figure S8A). Among these, Tyr242 and Asp246 are from helix α7′ of the opposing molecule in the EXD2-exo dimer, as described above.

To further examine whether the metal specificity and activity of EXD2 may be related to the structure of the active site, we determined crystal structures of EXD2-exo in complex with Mn^{2+}, Mg^{2+}, (d)GMP plus Mn^{2+} or (d)GMP plus Mg^{2+} (Figure 4B–H and Supplementary Figure S8B–H). The Mn^{2+} ion was found only in site M_A in the absence of dGMP, which is a mimic for the exonuclease product of DNA (Figure 4B). However, two Mn^{2+} ions were distinctly observed at both M_A and M_B sites in the presence of dGMP, although electron density representing dGMP was disordered in the structure (Figure 4D). Interestingly, Mg^{2+} ions were only found at site M_B regardless of the presence of dGMP (Figure 4C and E). The M_A site is occupied by two H_2O molecules when EXD2-exo is incubated with Mg^{2+} alone, while no ions (except for a single H_2O molecule) were observed at the M_A site when EXD2-exo was mixed with both Mg^{2+} and dGMP (Figure 4C and E). Moreover, when crystals are soaked in a solution containing both Mn^{2+} and Mg^{2+}, Mn^{2+} and Mg^{2+} ions are separately coordinated at only the M_A and M_B sites, respectively (Figure 4F). In summary, Mg^{2+} ions were not definitively located at the M_A site that is key for exonuclease activity, and this unexpected observation might explain why EXD2 is inactive toward DNA substrates in the presence of Mg^{2+} (Figure 2B and D). Interestingly, when crystals of EXD2-exo were soaked in a solution containing Mg^{2+} and GMP, a known ribonucleotide mimic of the RNase product, Mg^{2+} ions were located at both M_A and M_B sites (Figure 4G). We assume that the 2′-OH group of GMP might assist in this ion (M_A) capture. This hypothesis is supported by the fact that 2′-deoxyGMP, which lacks the OH group corresponding to the 'ordered water molecule', cannot bind to and assist in the capture of a second Mg^{2+}, resulting in only Mg^{2+} in the same site, as observed in unsoaked crystals. This result is consistent with the above data showing that EXD2 can cleave RNA in the presence of Mg^{2+} ion (Supplementary Figure S3). Likewise, Mn^{2+} ions were coordinated at both metal-binding sites in the presence of GMP (Figure 4H).

Structural basis for the metal and substrate specificity of EXD2-exo

Structural studies on EXD2-exo revealed that the metal coordination influences whether DNA or RNA substrates can be cleaved. We were therefore intrigued by the molecular basis by which EXD2-exo displays metal ion coordination and substrate (DNA or RNA) specificity, unlike WRN-exo, even though the two proteins share high structural similarity. The major difference between EXD2-exo and other DnaQ family exonucleases is that the active site of EXD2-exo is organized as a domain-swapped dimer (Figures 3B and 4; Supplementary Figure S6) (9,19–22). In particular, helix α7′ is one of the main structural elements provided by the opposing molecule in the EXD2-exo dimer. We speculate that this unusual active site organization might provide structural flexibility via helix α7′. Moreover, the highly conserved loop connecting helices α6′ and α7′ of EXD2-exo was disordered in all structures determined in this study, unlike the equivalent region in WRN-exo that is well ordered (Figure 3B) (9). This presumably suggests that helix α7′ may be more flexible in EXD2-exo than in WRN-exo. In fact, based on the crystal structures, helix α7 adopts two conformations, depending on metal coordination, unlike other DnaQ family exonucleases (9). As highlighted in Figure 4A, C and E, helix α7′ forms a slightly bent structure when Mn^{2+} is not bound to the M_A site. In more detail, when metal ions are absent, or when a sodium ion is bound to the M_A site, the distance between side chains Tyr242 and Asp246 in EXD2-exo is ∼6 Å, which seems to be too far to facilitate enzymatic action, consistent with the observed lack of exonuclease activity under these conditions (Figure 4A, C and E). However, the distance narrowed to ∼3.8 Å when manganese was bound at the M_A position (Figure 4B, D, F and H). The manganese ion was coordinated by the side chain of Asp246 and the hydroxyl group of Tyr242 through an ordered water molecule. These intimate interactions eventually affect the conformation of helix α7′, re-

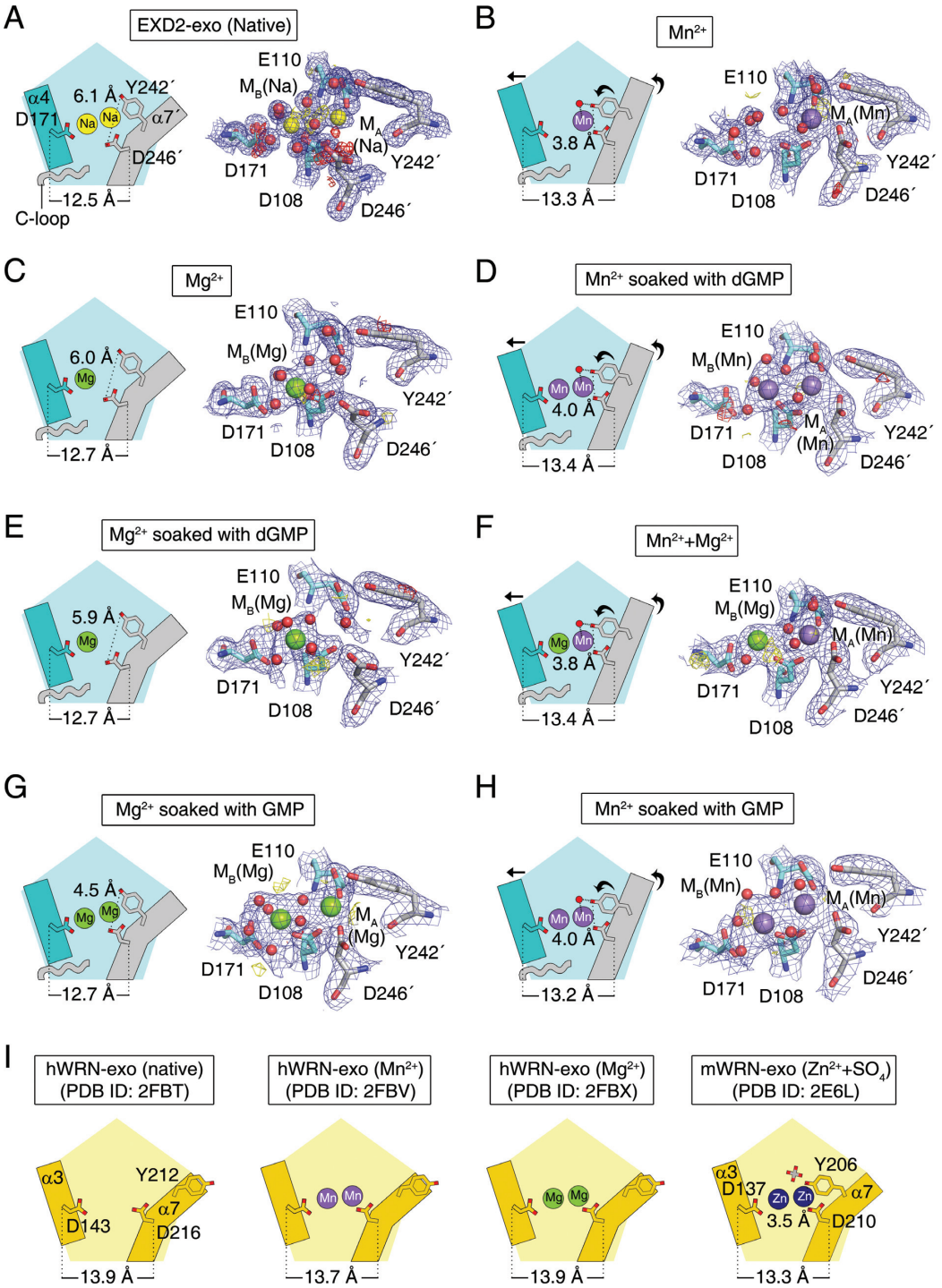

Figure 4. Structural basis for the metal and substrate specificities of EXD2-exo. (**A**–**H**) Schematic representations (left) based on the crystal structures (right) for native and metal ions and (d)GMP soaked structures showing the substrate discrimination of EXD2-exo resulting from metal coordination: (A) native crystal; (B) Mn^{2+}; (C) Mg^{2+}; (D) Mn^{2+} soaked with dGMP; (E) Mg^{2+} soaked with dGMP; (F) Mn^{2+} and Mg^{2+}; (G) Mg^{2+} soaked with GMP; (H) Mn^{2+} soaked with GMP. In right panels, 2Fo-Fc maps were contoured at 1.0 σ and Fo-Fc difference maps were contoured at 3.0 σ (yellow) and -3.0 σ (red). In left schematic figures, helices harboring active site residues involved in metal coordination are depicted as cylinders. The C-loop (residues 285–294) from the opposing protomer in the dimer is drawn in worm representation. Black arrows indicate conformation changes occurring when Mn^{2+} ions are bound to the M_A site in the catalytic domain of EXD2-exo (see text for detailed mechanism). Active site residues are shown with ball and stick representation in right panels. All structural elements provided by the opposing molecule in the EXD2-exo dimer are colored gray. Water, sodium, manganese and magnesium ions bound to the active site are shown as red, yellow, purple and green spheres, respectively. (**I**) Schematic representation of native and metal-soaked structures of human WRN-exo and Zn^{2+} soaked with sulfate (SO_4) structure of mouse WRN-exo shown in the same orientation as in (A). While Tyr212 in hWRN faces away from the active site, the conserved Tyr206 in mWRN is rotated toward the active site in the presence of sulphate ions (gray), which might act as a mimic of the substrate phosphate moiety. Color scheme of manganese and magnesium ions is the same as (A–H) and zinc ions bound to the active site of mWRN-exo are shown as blue spheres.

sulting in the straightening of this structural element. The distance of 3.8 Å is likely short enough to support enzyme catalysis by facilitating the cooperation of Tyr242, Asp246 and the ordered water molecule with the DNA substrate. When Mg^{2+} plus GMP is bound to EXD2-exo, although two Mg^{2+} ions are bound to the active site, this Mg^{2+} coordination is unable to induce an equivalent conformational change in helix α7′ (Figure 4G). We concluded that the 2′-hydroxyl group of GMP might replace the ordered water molecule, preventing the attraction of Tyr242 (Figure 4G).

The role of the C-segment in EXD2 metal selectivity

We therefore wondered why two magnesium ions could not be simultaneously coordinated by EXD2-exo in the presence of DNA as a substrate. Structure analyses indicated that the half coupling of Mg^{2+} to EXD2-exo might be due to insufficient space to accommodate two Mg^{2+} ions. As summarized in Figure 4A–H, the distance between Cα atoms of Asp171 and Asp246 is ∼12.5–12.7 Å when the α7 helix forms a kinked structure. However, this distance is increased to ∼13.4 Å when the helix adopts a straightened (extended) structure caused by the coordination of Mn^{2+} at the M_A site. Nevertheless, a distance of ∼13.4 Å might be insufficient for both Mg^{2+} ions to bind to the active site at the same time. In the previous structure of WRN-exo complexed with Mg^{2+} (PDB ID: 2FBX), the distance between equivalent atoms is ∼13.9 Å (Figure 4I). Even though EXD2-exo may have sufficient space, EXD2 might not be able to actively increase the distance to an appropriate size. The C-segment provided from the opposing molecule in the EXD2-exo dimer forms extensive contacts not only with helix α4 bearing Asp171, but also with the central β-sheet of the active site, and this may block the movement of helix α4, thereby hindering spatial expansion of the active site (Figures 4 and 5A; Supplementary Figure S7).

To test our hypothesis that the C-segment might play a pivotal role in regulating metal coordination in EXD2-exo, we generated truncated constructs excluding the C-segment (Figure 5B). Surprisingly, $EXD2^{76–284}$ lacking the C-loop that contacts the active site exhibited robust exonuclease activity with DNA as a substrate in the presence of Mg^{2+} as well as Mn^{2+}. By contrast, the $EXD2^{76–260}$ variant lacking the whole C-segment lost all ability to cleave DNA (Figure 5C). In fact, the sequence of $EXD2^{76–260}$ (185 residues) precisely corresponds to $WRN^{38–236}$ (199 residues) that possesses full exonuclease activity (9). Nevertheless, $EXD2^{76–260}$ completely lost exonuclease activity, implying that the C-segment (residues 260–295) is absolutely required for enzymatic activity of EXD2. Furthermore, we tested whether the C-segment supports the structural integrity of EXD2-exo by performing CD spectroscopy in the absence and presence of Mn^{2+}. As shown in Figure 5D, EXD2-exo lacking the C-segment displayed a reduction in melting temperature by ∼15°C compared with the wild-type protein, suggesting that the C-segment of EXD2 does indeed contribute to structural integrity and stability, unlike in other DEDDy family exonucleases. Interestingly, the addition of Mn^{2+} to the $EXD2^{76–284}$ variant recovered the melting temperature to that of the wild-type protein (Figure 5D, right). This is consistent with the data showing that $EXD2^{76–284}$ retained exonuclease activity in the presence of metal ions (Figure 5C). Collectively, these results suggest that the C-segment plays an important role in regulating the exonuclease activity not only by restricting metal ion coordination, but also by stabilizing the overall conformation.

The EXD2-exo substrate-binding site

As described above, even in the crystal structures of EXD2 in complex with (d)GMP, no apparent electron density corresponding to (d)GMP was found in the active site. Therefore, we investigated the probable substrate-binding region of EXD2-exo by superimposing the structure of EXD2-exo over that of trinucleotide-bound KF-exo, since the substrate-binding site of WRN-exo was analyzed previously using a similar approach (9). The overall geometry of residues in the active site of EXD2-exo is more similar to that in WRN-exo than in KF-exo (Figure 6A). However, the open conformation of Tyr212 (Tyr242 in EXD2-exo) in human WRN-exo was not observed in all structures of EXD2-exo (Figure 4I) (9). Rather, Tyr242 of EXD2-exo projects into the active site as shown in the structures of KF-exo (Tyr497, PDB ID: 1KFS) and mouse WRN-exo (Tyr206, PDB ID: 2E6L), and facilitates enzyme catalysis via an ordered water molecule and Mn^{2+} (Figure 6A) (8,19). In addition, the composite model suggests that the side chain of Arg226 directly stacks against the basic ring of the last nucleotide. The equivalent Arg190 in mWRN-exo forms a H-bond with the oxygen atom of the basic ring. Instead, the side chains of Phe473 in KF-exo and Cys191 in mWRN-exo play a similar role by positioning the last nucleotide. Lys185 in mWRN-exo is believed to be important for substrate binding (8). However, the equivalent residue in EXD2-exo (Lys221) is not visible in the electron density map and is presumably disordered. Significantly, based on the model, the Arg190 of helix α5 in EXD2-exo directly contacts the ribose ring of the first nucleotide of the trinucleotide and likely stabilizes the overall structure of the ligand (Figure 6A). Arg190 is absolutely conserved among members of the EXD2 family, but is absent from mWRN-exo and KF-exo (Figure 6A and Supplementary Figure S5).

We identified the substrate-binding region by alanine-scanning mutagenesis. As shown in Figure 6B and C, R226A single point mutants of EXD2-exo and tEXD2 lost all exonuclease activity, suggesting that Arg226 plays a key role in binding substrate nucleotides. Furthermore, as demonstrated for Lys185 in mWRN-exo (8), mutation of the equivalent Lys221 in EXD2 affected the exonuclease activity. Although this residue is not visible in the structure of EXD2-exo, it is obvious that it is also responsible for substrate recognition. Finally, mutation of Arg190 in both EXD2-exo and tEXD2 resulted in variants unable to cleave DNA substrates (Figure 6B and C).

Analysis of surface electrostatic potential revealed that EXD2-exo has a positively charged patch located just beneath the active sites (Figure 6D). This patch is mainly composed of Arg190, Arg195 and Arg197 from helix α5, and these residues are highly conserved among species (Supplementary Figure S5). We therefore infer that substrates to be cleaved might enter the catalytic site through this positively charged groove. The importance of Arg190 in substrate

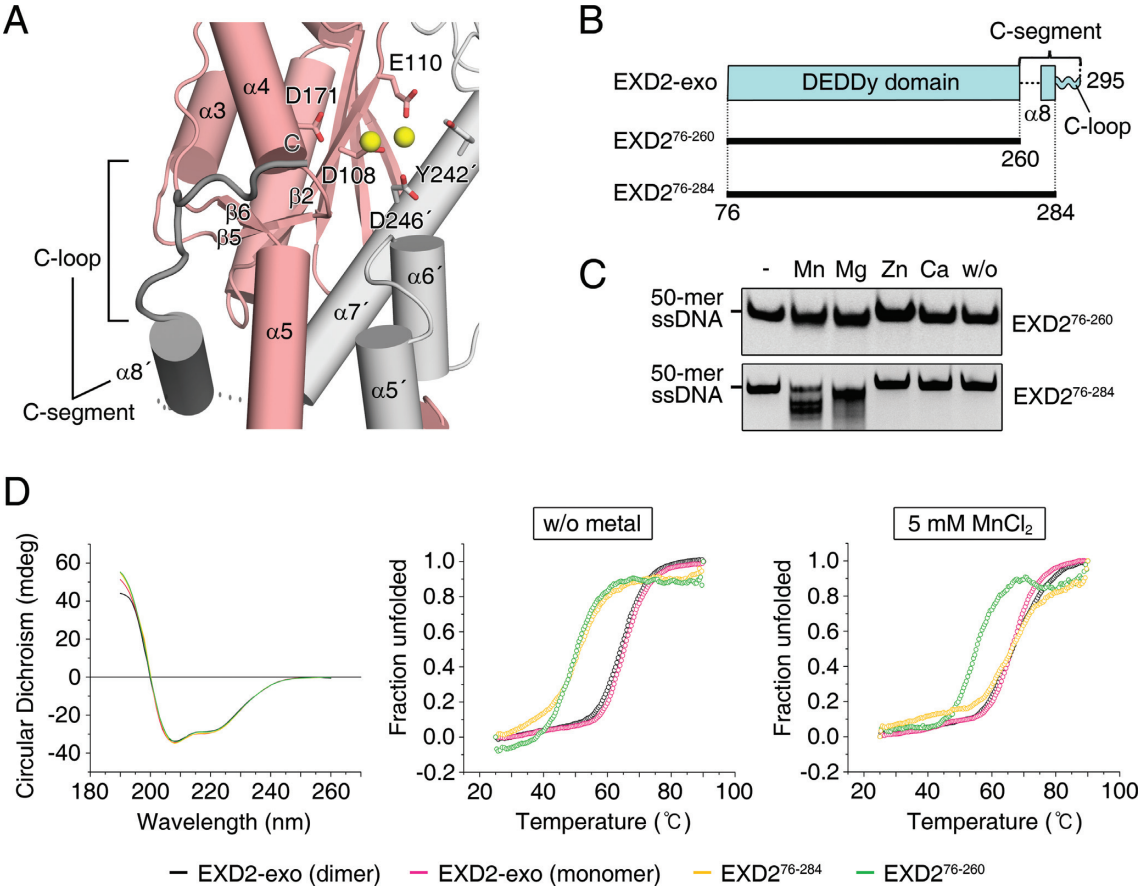

Figure 5. The C-segment is required for metal specificity and stability of the exonuclease domain. (**A**) Close-up view of the C-segment composed of α8 and the C-loop. The metal-binding active site of EXD2-exo is enclosed by the C-segment of the other molecule in the dimer and is restricted spatially. (**B**) To test the role of the C-segment in regulating the metal specificity, two truncated constructs ($EXD2^{76–260}$ and $EXD2^{76–284}$) were generated. (**C**) Metal cation-dependent exonuclease activities of $EXD2^{76–260}$ and $EXD2^{76–284}$. Protein (2.5 μM) was incubated with 0.25 μM 5-FAM-labeled 50-mer ssDNA for 1 h at 37°C and analyzed by non-denaturing TBE-PAGE. (**D**) Far-UV CD spectra of EXD2-exo (dimer and monomer), $EXD2^{76–260}$ and $EXD2^{76–284}$ from 190 to 260 nm (left). Thermal unfolding curves of EXD2-exo (dimer and monomer), $EXD2^{76–260}$ and $EXD2^{76–284}$ were measured by CD spectroscopy without and with 5 mM $MnCl_2$ (middle and right). Melting temperatures without $MnCl_2$ were as follows: EXD2-exo (dimer) = 64.6°C, EXD2-exo (monomer) = 65.2°C, $EXD2^{76–284}$ = 51.6°C, $EXD2^{76–260}$ = 50.3°C. Melting temperatures with 5 mM $MnCl_2$ were as follows: EXD2-exo (dimer) = 65.7°C, EXD2-exo (monomer) = 66.4°C, $EXD2^{76–284}$ = 65.6°C, $EXD2^{76–260}$ = 54.5°C.

binding was verified by biochemical data (Figure 6B and C). Additionally, we confirmed that mutation of Arg195 or Arg197 impaired enzymatic activity (Figure 6E). As mentioned above, the structure of helix α5 is extended, and this structural change seems to be essential for the formation of the EXD2-exo dimer (Figure 3A and B). In fact, if helix α5 is kinked, as is the case in WRN-exo and KF-exo, EXD2-exo forms a monomer, which could prevent EXD2-exo from forming a positively charged surface of sufficient length to guide substrate entry. In fact, mutation of equivalent residues in WRN and KF did not affect exonuclease activity (Supplementary Figure S9).

In contrast to WRN-exo and KF-exo, it is noteworthy that EXD2-exo has two active sites per dimer, related by 2-fold symmetry (Figure 6D). The distance between the two active sites is ∼46 Å. Unfortunately, at present it is difficult to explain why EXD2 has two catalytic sites that are closely associated, but future biochemical studies should address the role of this unusual catalytic domain arrangement. Nevertheless, it is clear that formation of the EXD2 dimer might be important for recruiting substrates to the active site by providing a positively charged patch of sufficient length.

DISCUSSION

In this study, we first determined the crystal structure of the human EXD2 exonuclease domain, revealing a novel structure in which the catalytic site is generated by chimeric arrangement of molecules in a domain-swapped dimer (Figure 2). Dimeric exonucleases have been proposed in several previous studies (24–27). However, this is the first report of an exonuclease domain that is only active when the enzyme is oligomerized. We also revealed the formation of a dimeric structure that might generate a positively charged groove of sufficient length to guide substrate entry in EXD2 (Figure 6). Moreover, this unusual active site organization and the presence of a unique C-segment could endow EXD2 with the novel ability to discriminate between DNA and RNA substrates via metal cation coordination (Figures 4 and 5). In fact, EXD2 only digests RNA and not DNA in the presence of Mg^{2+}, even though EXD2 hy-

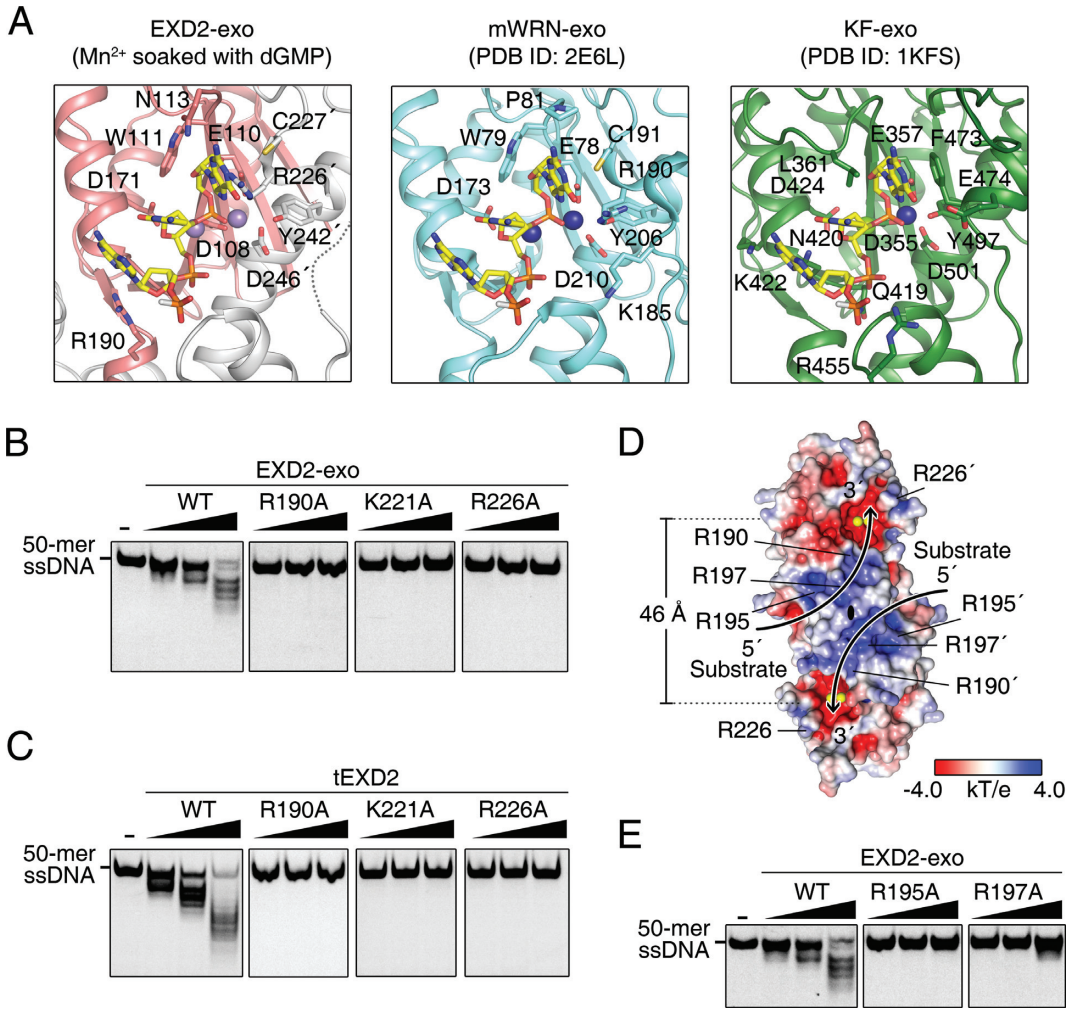

Figure 6. Dimerization of EXD2-exo is important for substrate binding. (**A**) Close-up views showing trinucleotide-bound EXD2-exo (left), mWRN-exo (middle) and KF-exo (right) in the same orientation to compare substrate-binding regions. Structural models were generated by superimposing structures of EXD2-exo (soaked with Mn^{2+} and dGMP, from this study) and mWRN-exo (PDB ID: 2E6L) with the structure of trinucleotide-bound KF-exo (PDB ID: 1KFS). In EXD2-exo, the two protomers are colored red and gray. The trinucleotide (yellow) and the side chains contacting the substrate are shown in ball-and-stick representation. Nitrogen and oxygen atoms are colored blue and red, respectively. (**B**) Exonuclease activity of EXD2-exo mutants (R190A, K221A and R226A). Mutant proteins (from the left, 0.5, 1 and 2 μM) were mixed with 5-FAM-labeled ssDNA as described in Figure 2B. (**C**) Exonuclease activity of tEXD2 mutants (R190A, K221A and R226A). The tEXD2 mutant proteins (from the left, 0.05, 0.1 and 0.2 μM) were analyzed as described in Figure 2B. (**D**) Electrostatic potential of the EXD2-exo molecular surface. The dimeric interface formed by the α5–α5′ crossover beneath the active sites generates a highly positively charged groove. Based on the trinucleotide-bound EXD2-exo model (A) combined with nuclease activity analyses (B and C), putative substrate-binding pathways are indicated by arrows. The electrostatic potential was calculated using the Adaptive Poisson-Boltzmann Solver (APBS) (39) and visualized (-4 kT/e, red, to +4 kT/e, blue) with PyMol (https://pymol.org/2/, version 1.7.4.4). (**E**) Exonuclease activity of EXD2-exo mutants (R195A and R197A). Experimental procedures were the same as in panel (B).

drolyzes both DNA and RNA when Mn^{2+} ions are bound (Figure 2 and Supplementary Figure S3). This is consistent with a previous study in which EXD2 was suggested to act as an RNase in the presence of Mg^{2+} in mitochondria (4). In addition to substrate discrimination, the dimeric organization might confer the ability to regulate catalytic activity because the exonuclease activity of EXD2 appears to be turned on only following self-association. Given that EXD2 is a membrane protein that is tightly anchored to the mitochondrial membrane, it might be geometrically difficult for molecules to associate with each other, suggesting that EXD2 might not always be active. It has not yet been tested whether the two EXD2 molecules are associated within the intra-mitochondrial membrane (homotypic interaction) or through inter-membrane interactions (heterotypic interaction) between two neighboring mitochondria (Supplementary Figure S10). In the latter case, EXD2 might be involved in mitochondrial tethering or mitochondrial dynamics such as fusion events (3,28–30). In any case, the geometrical restriction indicated herein implies that the activity of EXD2 could be modulated by unknown cellular factors.

EXD2 is an important player in the DNA double-strand break repair system (1). However, its biological role in the nucleus has been contradicted by its mitochondrial localization revealed in this and other studies (3,4). Thus, identification of its sub-mitochondrial localization is crucial to understanding its role in mitochondria. Mitochondrial matrix localization was recently demonstrated by fractiona-

tion, and it was concluded that it processes messenger RNA within mitochondria (4). Very recently, however, Hensen *et al.* provided further evidence of the OMM localization of EXD2 using proteinase K digestion with isolated mitochondria (3). In the present work, we confirmed OMM localization using a proximity labeling approach and APEX2-EM imaging (Figure 1). Furthermore, we revealed that EXD2 contains an N-terminal single TM domain that anchors it to the OMM and a C-terminal domain that is mainly localized to the cytosolic face of the OMM (Figure 1 and Supplementary Figure S1). These results suggest that the exonuclease domain of EXD2 may have a novel function at the OMM that has not yet been proposed.

Due to the absence of known DNA populations near the OMM, we propose that EXD2 might be involved in the processing of RNA in the vicinity of the OMM. In particular, we speculate that EXD2 might be involved in the biogenesis of Piwi-interacting RNA (piRNA) since the OMM is recognized as a hub for processing piRNA, which is crucial for germ cell development (29,31). Our hypothesis is supported by the published data showing that germ stem cell attrition is significantly accelerated in EXD2-deficient ovaries of drosophila (4). Moreover, EXD2 is also highly expressed in reproductive organs in human (32). In the Gtex portal (33), EXD2 expression is reportedly higher in testes and brain than in other tissues. Because many piRNA biogenesis proteins, such as PIWIL1, TDRKH and MitoPLD, are overexpressed in testes for the generation of the large amounts of piRNA needed to protect the genetic stability of germ cell lines (34), a similar testis-specific expression pattern of EXD2 in humans could indicate its possible involvement in piRNA biogenesis. In the process of piRNA biogenesis, we further speculate that EXD2 could function as a Trimmer, which digests the 3′ ends of pre-piRNA molecules, although PNLDC1 (35) and EXD3 (also known as Nibbler in drosophila) (36) have been proposed to be Trimmers in different models. As regards its possible role in piRNA biogenesis, it is intriguing to suggest that the homotypic dimer of EXD2 may engage in functional interactions with the homodimeric complex of MitoPLD at the OMM, which also contains a signal anchoring the TM helix at the N-terminus (37). The heterotypic interaction mode of EXD2 might function at the inter-mitochondrial cement, which is observed in spermatogenesis in mammals (38). Future work will be required to address the role that dimerization of the EXD2 exonuclease domain may play in regulating physiological function.

DATA AVAILABILITY

Atomic coordinates and structure factors are deposited in the Protein Data Bank with accession codes: 6K17 (native EXD2-exo), 6K18 (soaked in Mn^{2+}), 6K19 (soaked in Mg^{2+}), 6K1A (soaked in Mn^{2+} and Mg^{2+}), 6K1B (soaked in Mn^{2+} and dGMP), 6K1C (soaked in Mg^{2+} and dGMP), 6K1D (soaked in Mn^{2+} and GMP) and 6K1E (soaked in Mg^{2+} and GMP).

SUPPLEMENTARY DATA

Supplementary Data are available at NAR Online.

ACKNOWLEDGEMENTS

We thank staff from beamlines 5C and 11C at the Pohang Accelerator Laboratory (PAL) for assistance with X-ray diffraction data collection. The authors also thank Prof. Taejoon Kwon (UNIST) and Prof. Mihye Lee (Soonchunhyang Univ.) for helpful discussion of EXD2 function in animal models.

Author Contributions **:** C.L. and H.W.R. conceived the study. J.P. and S.Y.L. performed all biochemical experiments with help from H.J., M.G.K., L.V.H., M.M., J.K.S., Y.J. and K.M. J.P., H.J. and C.L. determined the crystal structures. J.P., S.Y.L., H.W.R. and C.L. prepared the manuscript.

FUNDING

Cell Logistics Research Center [2016R1A5A1007318]; Basic Research Program, National Research Foundation of Korea [NRF-2019R1A2C3008463]; Korea Health Technology R&D Project through the Korea Health Industry Development Institute (KHIDI), funded by the Ministry of Health & Welfare, Republic of Korea [HI18C1395]; Institute for Basic Science [IBS-R022-D1]. Funding for open access charge: Cell Logistics Research Center, National Research Foundation of Korea [2016R1A5A1007318].

Conflict of interest statement. None declared.

REFERENCES

1. Broderick,R., Nieminuszczy,J., Baddock,H.T., Deshpande,R., Gileadi,O., Paull,T.T., McHugh,P.J. and Niedzwiedz,W. (2016) EXD2 promotes homologous recombination by facilitating DNA end resection. *Nat. Cell Biol.*, **18**, 271–280.
2. Thul,P.J., Akesson,L., Wiking,M., Mahdessian,D., Geladaki,A., Ait Blal,H., Alm,T., Asplund,A., Bjork,L., Breckels,L.M. *et al.* (2017) A subcellular map of the human proteome. *Science*, **356**, 815–820.
3. Hensen,F., Moretton,A., van Esveld,S., Farge,G. and Spelbrink,J.N. (2018) The mitochondrial outer-membrane location of the EXD2 exonuclease contradicts its direct role in nuclear DNA repair. *Sci. Rep.*, **8**, 5368.
4. Silva,J., Aivio,S., Knobel,P.A., Bailey,L.J., Casali,A., Vinaixa,M., Garcia-Cao,I., Coyaud,E., Jourdain,A.A., Perez-Ferreros,P. *et al.* (2018) EXD2 governs germ stem cell homeostasis and lifespan by promoting mitoribosome integrity and translation. *Nat. Cell Biol.*, **20**, 162–174.
5. Lee,S.Y., Kang,M.G., Shin,S., Kwak,C., Kwon,T., Seo,J.K., Kim,J.S. and Rhee,H.W. (2017) Architecture mapping of the inner mitochondrial membrane proteome by chemical tools in live cells. *J. Am. Chem. Soc.*, **139**, 3651–3662.
6. Sosinsky,G.E., Giepmans,B.N.G., Deerinck,T.J., Gaietta,G.M. and Ellisman,M.H. (2007) *Methods in Cell Biology*. Academic Press, San Diego, Vol. **79**, pp. 575–591.
7. Schnell,U., Dijk,F., Sjollema,K.A. and Giepmans,B.N. (2012) Immunolabeling artifacts and the need for live-cell imaging. *Nat. Methods*, **9**, 152–158.
8. Choi,J.M., Kang,S.Y., Bae,W.J., Jin,K.S., Ree,M. and Cho,Y. (2007) Probing the roles of active site residues in the 3′-5′ exonuclease of the Werner syndrome protein. *J. Biol. Chem.*, **282**, 9941–9951.
9. Perry,J.J., Yannone,S.M., Holden,L.G., Hitomi,C., Asaithamby,A., Han,S., Cooper,P.K., Chen,D.J. and Tainer,J.A. (2006) WRN exonuclease structure and molecular mechanism imply an editing role in DNA end processing. *Nat. Struct. Mol. Biol.*, **13**, 414–422.
10. Lee,S.Y., Kang,M.G., Park,J.S., Lee,G., Ting,A.Y. and Rhee,H.W. (2016) APEX fingerprinting reveals the subcellular localization of proteins of interest. *Cell Rep.*, **15**, 1837–1847.
11. Lee,S.Y., Lee,H., Lee,H.K., Lee,S.W., Ha,S.C., Kwon,T., Seo,J.K., Lee,C. and Rhee,H.W. (2016) Proximity-directed labeling reveals a

new rapamycin-induced heterodimer of FKBP25 and FRB in live cells. *ACS Cent. Sci.*, **2**, 506–516.
12. Otwinowski,Z. and Minor,W. (1997) Processing of X-ray diffraction data collected in oscillation mode. *Methods in enzymology*. Elsevier, San Diego, Vol. **276**, pp. 307–326.
13. McCoy,A.J., Grosse-Kunstleve,R.W., Adams,P.D., Winn,M.D., Storoni,L.C. and Read,R.J. (2007) Phaser crystallographic software. *J. Appl. Crystallogr.*, **40**, 658–674.
14. Emsley,P., Lohkamp,B., Scott,W.G. and Cowtan,K. (2010) Features and development of Coot. *Acta Crystallogr. D. Biol. Crystallogr.*, **66**, 486–501.
15. Adams,P.D., Afonine,P.V., Bunkoczi,G., Chen,V.B., Davis,I.W., Echols,N., Headd,J.J., Hung,L.W., Kapral,G.J., Grosse-Kunstleve,R.W. *et al.* (2010) PHENIX: a comprehensive Python-based system for macromolecular structure solution. *Acta Crystallogr. D. Biol. Crystallogr.*, **66**, 213–221.
16. Shore,G.C., Mcbride,H.M., Millar,D.G., Steenaart,N.A.E. and Nguyen,M. (1995) Import and insertion of proteins into the mitochondrial outer-membrane. *Eur. J. Biochem.*, **227**, 9–18.
17. Rapaport,D. (2003) Finding the right organelle. Targeting signals in mitochondrial outer-membrane proteins. *EMBO Rep.*, **4**, 948–952.
18. Lam,S.S., Martell,J.D., Kamer,K.J., Deerinck,T.J., Ellisman,M.H., Mootha,V.K. and Ting,A.Y. (2015) Directed evolution of APEX2 for electron microscopy and proximity labeling. *Nat. Methods*, **12**, 51–54.
19. Brautigam,C.A. and Steitz,T.A. (1998) Structural principles for the inhibition of the 3′-5′ exonuclease activity of Escherichia coli DNA polymerase I by phosphorothioates. *J. Mol. Biol.*, **277**, 363–377.
20. Zuo,Y., Wang,Y. and Malhotra,A. (2005) Crystal structure of Escherichia coli RNase D, an exoribonuclease involved in structured RNA processing. *Structure*, **13**, 973–984.
21. Breyer,W.A. and Matthews,B.W. (2000) Structure of Escherichia coli exonuclease I suggests how processivity is achieved. *Nat. Struct. Biol.*, **7**, 1125–1128.
22. Hamdan,S., Carr,P.D., Brown,S.E., Ollis,D.L. and Dixon,N.E. (2002) Structural basis for proofreading during replication of the Escherichia coli chromosome. *Structure*, **10**, 535–546.
23. Cull,M.G. and Schatz,P.J. (2000) Biotinylation of proteins in vivo and in vitro using small peptide tags. *Methods in Enzymology*. Elsevier, San Diego, USA, Vol. **326**, pp. 430–440.
24. Brucet,M., Querol-Audi,J., Serra,M., Ramirez-Espain,X., Bertlik,K., Ruiz,L., Lloberas,J., Macias,M.J., Fita,I. and Celada,A. (2007) Structure of the dimeric exonuclease TREX1 in complex with DNA displays a proline-rich binding site for WW Domains. *J. Biol. Chem.*, **282**, 14547–14557.
25. Zuo,Y., Zheng,H., Wang,Y., Chruszcz,M., Cymborowski,M., Skarina,T., Savchenko,A., Malhotra,A. and Minor,W. (2007) Crystal structure of RNase T, an exoribonuclease involved in tRNA maturation and end turnover. *Structure*, **15**, 417–428.
26. Hsiao,Y.Y., Nakagawa,A., Shi,Z., Mitani,S., Xue,D. and Yuan,H.S. (2009) Crystal structure of CRN-4: implications for domain function in apoptotic DNA degradation. *Mol. Cell. Biol.*, **29**, 448–457.
27. Wu,M.S., Reuter,M., Lilie,H., Liu,Y.Y., Wahle,E. and Song,H.W. (2005) Structural insight into poly(A) binding and catalytic mechanism of human PARN. *EMBO J.*, **24**, 4082–4093.
28. Chan,D.C. (2012) Fusion and fission: interlinked processes critical for mitochondrial health. *Annu. Rev. Genet.*, **46**, 265–287.
29. Choi,S.Y., Huang,P., Jenkins,G.M., Chan,D.C., Schiller,J. and Frohman,M.A. (2006) A common lipid links Mfn-mediated mitochondrial fusion and SNARE-regulated exocytosis. *Nat. Cell Biol.*, **8**, 1255–1262.
30. Mishra,P. and Chan,D.C. (2014) Mitochondrial dynamics and inheritance during cell division, development and disease. *Nat. Rev. Mol. Cell Biol.*, **15**, 634–646.
31. Weick,E.M. and Miska,E.A. (2014) piRNAs: from biogenesis to function. *Development*, **141**, 3458–3471.
32. Uhlen,M., Fagerberg,L., Hallstrom,B.M., Lindskog,C., Oksvold,P., Mardinoglu,A., Sivertsson,A., Kampf,C., Sjostedt,E., Asplund,A. *et al.* (2015) Tissue-based map of the human proteome. *Science*, **347**, 1260419.
33. Su,A.I., Wiltshire,T., Batalov,S., Lapp,H., Ching,K.A., Block,D., Zhang,J., Soden,R., Hayakawa,M., Kreiman,G. *et al.* (2004) A gene atlas of the mouse and human protein-encoding transcriptomes. *Proc. Natl. Acad. Sci. U.S.A.*, **101**, 6062–6067.
34. Anastasakis,D., Skeparnias,I., Shaukat,A.N., Grafanaki,K., Kanellou,A., Taraviras,S., Papachristou,D.J., Papakyriakou,A. and Stathopoulos,C. (2016) Mammalian PNLDC1 is a novel poly(A) specific exonuclease with discrete expression during early development. *Nucleic Acids Res.*, **44**, 8908–8920.
35. Izumi,N., Shoji,K., Sakaguchi,Y., Honda,S., Kirino,Y., Suzuki,T., Katsuma,S. and Tomari,Y. (2016) Identification and functional analysis of the pre-piRNA 3′ trimmer in silkworms. *Cell*, **164**, 962–973.
36. Hayashi,R., Schnabl,J., Handler,D., Mohn,F., Ameres,S.L. and Brennecke,J. (2016) Genetic and mechanistic diversity of piRNA 3′-end formation. *Nature*, **539**, 588–592.
37. Ipsaro,J.J., Haase,A.D., Knott,S.R., Joshua-Tor,L. and Hannon,G.J. (2012) The structural biochemistry of Zucchini implicates it as a nuclease in piRNA biogenesis. *Nature*, **491**, 279–283.
38. Chuma,S., Hosokawa,M., Tanaka,T. and Nakatsuji,N. (2009) Ultrastructural characterization of spermatogenesis and its evolutionary conservation in the germline: germinal granules in mammals. *Mol. Cell. Endocrinol.*, **306**, 17–23.
39. Baker,N.A., Sept,D., Joseph,S., Holst,M.J. and McCammon,J.A. (2001) Electrostatics of nanosystems: application to microtubules and the ribosome. *Proc. Natl. Acad. Sci. U.S.A.*, **98**, 10037–10041.